Hillslopes record the growth and decay of landscapes

Martin D. Hurst[1, 2*], Simon M. Mudd[1], Mikael Attal[1], George Hilley[3]

[1]School of Geosciences, University of Edinburgh, Drummond Street, Edinburgh, United Kingdom, EH8 9XP.

[2]British Geological Survey, Keyworth, Nottingham, United Kingdom, NG12 5GG.

[3]Department of Geological and Environmental Sciences, Stanford University, 397 Panama Mall, Stanford, CA, 94305-2210, United States.

*Corresponding Author (email: mhurst@bgs.ac.uk)

One Sentence Summary:

Hillslope morphology indicates whether a landscape is undergoing rejuvenation or decay, and consequently may be used to quantitatively derive changes in tectonic rates.

Abstract:

The Earth's surface archives the combined history of tectonics and erosion, which tend to roughen landscapes, and sediment transport and deposition, which smooth them. We analyzed hillslope morphology in the tectonically active Dragon's Back Pressure Ridge in California, USA, to assess whether tectonic uplift history can be reconstructed using measurable attributes of hillslope features within landscapes. Hilltop curvature and hillslope relief mirror measured rates of vertical displacement caused by tectonic forcing, and their relationships are consistent with those expected when idealizing hillslope transport as a non-linear diffusion process. Hilltop curvature lags behind relief in its response to changing erosion rates, allowing growing landscapes to be distinguished from decaying landscapes. Numerical modeling demonstrates that hillslope morphology may be used to infer changes in tectonic rates.

Main Body:

Hillslope morphology is a first-order indicator of landscape change, with great potential for interrogating landscapes in tectonically active settings (*1-3*). Under the condition that erosion rates have adjusted to tectonic uplift, landscape morphology can be used to infer uplift rates (*4*). Until recently, efforts have focused on inferring rates of base-level fall from channel profiles; hillslopes were generally considered insensitive to rapid base-level fall since they become invariantly steep and planar in such context (*5*). Advances in the quality of digital topographic data have recently led to new techniques allowing interpretation of hillslope morphology as a first-order indicator of change in boundary conditions, even in rapidly uplifted landscapes (*1-3*). In the limiting case that channels respond more rapidly to changes in uplift rates than do hillslopes, the history of tectonic rates may be faithfully archived in the profile form of hillslopes (*6*). Hilltop curvature (C_{HT}) and mean hillslope gradient (S) are expected to predictably vary with relative base-level lowering rates (hereafter equated with tectonic uplift rate, U) providing hilltops remain soil-mantled (*2, 7*). We study hillslope morphology at the Dragon's Back Pressure Ridge (DBPR), located along the San Andreas Fault (SAF), California, USA. Small catchments (<400 m long) trending perpendicular to the fault are cut into poorly consolidated sediments of the Paso Robles formation that is readily transportable as soil (*8*). Geological mapping reveals that these sediments are progressively folded as a monocline to the northwest. Surface structures exposed within the North American Plate and magnetotelluric profiles suggest that the SAF is offset in the shallow subsurface and that this offset remains stationary with respect to the North American Plate. Taken together, these observations indicate that flat-lying sediments southwest of the DBPR are progressively deformed as strike-slip motion moves them into and through the deformation zone created by this offset (Fig. 1a). Topography along the DBPR reflects translation through the fixed uplift zone at a rate equal to the mean slip rate along the SAF (33 mm a^{-1}), allowing a space-for-time substitution to analyze topography as a result of the integrated uplift history along the landform. As such, uplift increases rapidly from SE to NW along the landform, peaking 1200 m from the SE tip of the ridge (30 ka) and declining by 2000 m (60 ka) (Fig. 1a) (*8*). Additionally, it has been demonstrated that the fluvial system rapidly communicates changes in uplift rates to hillslopes, which is a limiting condition required to examine hillslope responses to changing tectonic rates (*8*).

In steep, rapidly eroding terrain, hillslope gradient is often invariant (*5, 9*), an observation consistent with geomorphic transport models in which sediment flux increases nonlinearly with hillslope gradient and tends to infinity as gradient approaches a critical slope, S_C *(2, 10, 11)*. When tectonic uplift is balanced by surface lowering rates (hereafter referred to as steady-state), a relationship can be derived from this flux law between two dimensionless topographic measures: an apparent dimensionless erosion rate E^* and dimensionless relief R^* (*7*) (see supplementary material):

$$E^* = \frac{2\,C_{HT}\,L_H}{S_C} \qquad [1]$$

$$R^* = \frac{S}{S_C}; \qquad S < S_C \qquad [2]$$

where L_H is horizontal hillslope length. Changes in E^* and R^* are primarily driven by changes in C_{HT} and S, respectively. As E^* becomes large, R^* asymptotically approaches unity, indicating that mean slopes approach S_C at high uplift rates (Fig. 2a; dashed line). When the steady-state assumption is violated, deviation from the steady-state relationship (Fig. 2a; dashed line) has been hypothesized to reflect the adjustment of hillslope profiles to changes in relative base-level lowering rates (*6*). Therefore, we calculate E^* and R^* from high-resolution topographic data (see supplementary material for details) by quantifying S, C_{HT} and L_H to reveal landscape history in relation to changing uplift (*2*).

S, C_{HT} and L_H all increase in response to increased erosion rates (Fig. 1). S attains maximum values by 900 m (27 ka) along the landform and remains high until 2700 m (82 ka), suggesting that S is limited by landsliding in these areas as previously observed (*8*). By 750 m (23 ka), L_H increases to 30 m and remains approximately constant until 2700 m (82 ka). Uplift rates are high (> 1mm a^{-1}) at 900-1800 m (27-55 ka); in this zone, C_{HT} increases to a maximum value 750 m (23 ka) after uplift has declined.

We used S, C_{HT}, and L_H to calculate E^* and R^*, fixing $S_C = 0.8$ so that R^* cannot exceed unity (S should not exceed S_C). We observed systematic deviations between the measured values and those expected for steady-state hillslopes (Fig. 2a). Initially, increasing S, L_H and C_{HT},

elevate R^* and E^* respectively. R^* does not notably increase after 25 ka as hillslope gradient approaches S_C. Increasing C_{HT} raises E^* even after uplift ceases at 55 ka. From 80 ka onwards, both E^* and R^* decline gradually; however, E^* values are larger for a given R^* value than would be predicted based on the steady-state model. This pattern suggests that changes in C_{HT} (and hence E^*) lag behind S (and hence R^*). The result is tectonically induced hysteresis in hillslope form: high-relief, low-C_{HT}, and low-relief, high-C_{HT}, hillslopes are associated with active and waning tectonic uplift, respectively.

We constructed a one-dimensional numerical model of hillslope evolution to determine if the observed hysteresis could be explained by the lag in hillslope response to changes in base-level lowering rates (see supplementary material). The model used a time-dependent uplift pulse idealized as a Gaussian function with the timing (t_{max}^*), standard deviation (t_{std}^*) and magnitude (U_{max}^*) of uplift treated as model parameters. L_H and the transport coefficient D (see supplementary material) were fixed for the modeled hillslope. A Monte Carlo approach was used to find the most likely combination of these parameters according to the misfit between values of R^* and E^* derived from the DBPR topography and those calculated at corresponding model-time values in the forward model.

The resulting distribution of apparent uplift is shown in Fig. 3a. Dimensionalization of the best fit modeled uplift field uses D = 0.0086 m^2 a^{-1} as previously derived for the study site (*12*), and the similarity in magnitude of modeled U with the independently-derived mapped uplift field (*8*) supports this value. The model reasonably explains the distribution of hillslope morphology, as shown by the similarity between E^* derived from topography and the modeled hillslope through time (Fig. 3b). Although first-order features of hillslopes within the DBPR were captured using the model, several key features remain unexplained.

First, the inferred U^* distribution implicitly equates changes in base-level lowering rate with changes in rock uplift rate. Channels adjust rapidly but not instantaneously to the waning of uplift (*8*). This delayed channel response introduces an additional 15-20 ka (t^* = 0.14-0.19) lag between changes in uplift and relative base-level fall along hillslopes, similar to the offset between their mapped uplift field and the most likely distribution of U^* derived from the model

(Fig. 3a). The modeled t_{std}^* values were larger than those observed, with apparent uplift distributed throughout the model run (Fig. 3a).

Secondly, peak E^* values are smaller than E^* derived from the topography (Fig. 3b). This likely reflects the choice of a modeled Gaussian uplift pulse that is smoother than the documented uplift distribution at the DBPR.

Thirdly, toward the NW end of the DBPR (beyond 2700 m / 80 ka), R^* is generally smaller than model predictions (Fig. 3c). The mismatch could be due to high transport rates in the study area associated with processes that are not replicated in the model, such as debris-flows, landslides, and erosion by overland flow (see Fig. S2), which have been interpreted as a possible cause for variation in channel concavities within and beyond the uplift zone (*8*).

Finally we integrated the modeling results with field observations in a conceptual framework for the temporal evolution of DBPR (Fig. 2b). Accelerated uplift drives erosional adjustment that propagates into a landscape. Channel erosion ensues, with a concomitant delay in hillslope response, so relief can grow without a commensurate change in C_{HT} and thus E^*, leading to data lying above the steady-state E^* vs. R^* curve. Once uplift stops, channels rapidly become gentler (*8*) whereas again hillslopes and hilltops are slower to respond, leading to points lying below the steady E^* vs. R^* curve. This hysteresis in has important implications for the interpretation of transient hillslopes, providing a means to discriminate growing and decaying landscapes based on hillslope topography alone. Our findings highlight the potential to distinguish active faults in remote settings, quantify the distribution of fault-related uplift and delineate zones with high landslide risk (i.e., zones with high uplift rate, steep landscape and/or proximity to active faults). Such an approach will be best suited to landscapes where hillslopes have a response time that is longer than that of the channel network, but not so long that channels effectively become decoupled from their base-level. Alternatively where the response time of the channel network is very long, hillslopes may be able to track spatial variation in relative base-level (*2*) and provide a complementary test to channel-based erosion rate metrics.

Figure Captions:

Figure 1: Study site and hillslope morphology: (a) Shaded relief image of DBPR adjacent to the SAF (UTM zone 11N projection; (E)astings and (N)orthings in meters). Contours show distribution of surface uplift derived by geological mapping of deformed sedimentary beds (*8*) and black lines depict mapped hilltops. (b) Distribution of surface metrics sampled from hilltops in (a). Shaded regions show standard deviation and solid lines are standard errors about bin means. Space-for-time substitution is based on 0.033 m a^{-1} slip rate on the SAF (*8*). *S* appears limited by 900m along the DBPR, whilst C_{HT} continues to increase suggesting rising erosion rates.

Figure 2: Hysteresis in hillslope morphology: (a) Variation in E^* and R^* with distance towards NW along DBPR. Dashed line indicates theoretical relationship for steady-state hillslopes. Error bars propagated from standard errors in Fig. 1. Space-for-time substitution is based on 0.033 m a^{-1} slip rate on the SAF (*8*). The morphological evolution of hillslopes is distinct for adjustment during uplift versus relaxation after uplift has ceased. (b) Schematic diagram illustrating landscape response to the onset and conclusion of uplift and the expected distribution of E^* vs. R^* (inset plot). Values for E^* vs. R^* reflect hillslope profiles highlighted in red on the schematic plot. Uplift triggers increased erosion rates in channels which dissect the original surface. A wave-like signal propagates onto the hillslopes, causing steepening (20-40 ka). Subsequently, the hilltops respond by becoming sharper (60-80 ka). At 60 ka uplift ceases and channel slopes decrease (*8*). Hillslope gradients and hilltop curvature both reduce gradually in response.

Figure 3: Modeled Uplift: (a) Distribution of U^* as a function of t^*. Solid black line represents the mapped uplift field normalized following Equation S3c (using D = 0.0086 m^2 a^{-1} (*12*) and L_H = 30 m) and slip rate of 0.033 m a^{-1}. Grey line is the Gaussian function for apparent uplift (base-level fall) providing best fit to observed topography from probability densities with mean values (± 1σ) of $U_{max}{}^*$ = 20.89 (±0.6), $t_{max}{}^*$ = 0.621 (±0.001) and $t_{std}{}^*$ = 0.490 (± 0.015). (b) Distribution of E^* through t^*: topography-derived (Equation 5b) and modeled E^* (Pearson's correlation test gives R^2 = 0.78). (c) Distribution of modeled and measured R^* through t^*. (d) E^* from topography and modeled hillslopes as a function of model-derived apparent uplift U^* through t^*. Hysteresis is recorded such that during accelerating uplift and topographic growth E^* lags behind U^* whilst during landscape relaxation E^* lags behind a declining U^*.

References

1. R. A. DiBiase, A. M. Heimsath, K. X. Whipple, Hillslope response to tectonic forcing in threshold landscapes. *Earth Surface Processes and Landforms* **37**, 855 (2012).
2. M. D. Hurst, S. M. Mudd, R. Walcott, M. Attal, K. Yoo, Using hilltop curvature to derive the spatial distribution of erosion rates. *Journal of Geophysical Research-Earth Surface* **117**, F02017 (2012).
3. M. D. Hurst, S. M. Mudd, K. Yoo, M. Attal, R. Walcott, Influence of lithology on hillslope morphology and response to tectonic forcing in the northern Sierra Nevada of California. *Journal of Geophysical Research-Earth Surface*, 118, 1 (2013).
4. A. C. Whittaker, How do landscapes record tectonics and climate? *Lithosphere* **4**, 160 (2012).
5. R. A. DiBiase, K. X. Whipple, A. M. Heimsath, W. B. Ouimet, Landscape form and millennial erosion rates in the San Gabriel Mountains, CA. *Earth and Planetary Science Letters* **289**, 134 (2010).
6. S. M. Mudd, D. J. Furbish, Responses of soil-mantled hillslopes to transient channel incision rates. *Journal of Geophysical Research-Earth Surface* **112**, (2007).
7. J. J. Roering, J. T. Perron, J. W. Kirchner, Functional relationships between denudation and hillslope fonn and relief. *Earth and Planetary Science Letters* **264**, 245 (2007).
8. G. E. Hilley, J. R. Arrowsmith, Geomorphic response to uplift along the Dragon's Back pressure ridge, Carrizo Plain, California. *Geology* **36**, 367 (2008).
9. S. A. Binnie, W. M. Phillips, M. A. Summerfield, L. K. Fifield, Tectonic uplift, threshold hillslopes, and denudation rates in a developing mountain range. *Geology* **35**, 743 (2007).
10. D. J. Andrews, R. C. Bucknam, Fitting degradation of shoreline scarps by a nonlinear diffusion-model. *Journal of Geophysical Research* **92**, 12857 (1987).
11. J. J. Roering, J. W. Kirchner, W. E. Dietrich, Evidence for nonlinear, diffusive sediment transport on hillslopes and implications for landscape morphology. *Water Resources Research* **35**, 853 (1999).
12. J. R. Arrowsmith, D. D. Rhodes, D. D. Pollard, Morphologic dating of scarps formed by repeated slip events along the San Andreas Fault, Carrizo Plain, California. *Journal of Geophysical Research* **103**, 10141 (1998).
13. J. S. Evans, A. T. Hudak, A Multiscale Curvature Algorithm for Classifying Discrete Return LiDAR in Forested Environments. *Geoscience and Remote Sensing, IEEE Transactions* **45**, 1029 (2007).
14. A. Buades, B. Coll, J. M. Morel, A non-local algorithm for image denoising. *Computer Vision and Pattern Recognition, IEEE Computer Society Conference.* **2**, 60 (2005).
15. R. Jyotsna, P. K. Haff, Microtopography as an indicator of modern hillslope diffusivity in arid terrain. *Geology* **25**, 695 (1997).
16. N. Metropolis, A. W. Rosenbluth, M. N. Rosenbluth, A. H. Teller, E. Teller, Equation of state calculations by fast computing machines. *The Journal of Chemical Physics* **21**, 1087 (1953).
17. A. Gelman, J. B. Carlin, H. S. Stern, D. B. Rubin, *Bayesian data analysis*. Chapman and Hall, (2003).
18. B. A. Berg, *Introduction to markov chain monte carlo simulations and their statistical analysis.* World Scientific (2004).
19. W. K. Hastings, Monte Carlo sampling methods using Markov chains and their applications. *Biometrika* **57**, 97 (1970).

Acknowledgements:

This work was supported by a National Environmental Research Council NE/G524128/1 awarded to Hurst; and NE/H001174/1 and a grant from the Carnegie Trust for the Universities of Scotland to Mudd. Thanks to J. Roering, D. Lague and M. Ellis for helpful discussions. Three anonymous reviewers provided comments which greatly improved the manuscript.

Supplementary Materials:

211

Supplementary Materials for

Hillslopes record the growth and decay of landscapes

Martin D. Hurst, Simon M. Mudd, Mikael Attal and George Hilley

correspondence to: mhurst@bgs.ac.uk

This PDF file includes:

Materials and Methods

Hillslope Model

The evolution of a one-dimensional hillslope follows:

$$\frac{d\zeta}{dt} = \rho^* U - E = \rho^* U - \frac{dq_s}{dx} \quad \text{[S1]}$$

such that surface elevation ζ changes through time t where U is surface uplift rate [L T^{-1}], ρ^* is the density ratio between bedrock and dry soil, E is erosion rate [L T^{-1}], x is distance along the hillslope and q_s is volumetric sediment flux per unit width [L^2 T^{-1}] (dimensions of [L]ength, [M]ass and [T]ime denoted with square brackets). Sediment flux in steep, soil mantled landscapes can be modeled using (*10, 11*):

$$q_s = \frac{-DS}{1-(S/S_C)^2} \quad \text{[S2]}$$

where D is a transport coefficient [L^2 T^{-1}], S is hillslope gradient [L L^{-1}] and S_C [L L^{-1}] is a critical hillslope gradient toward which sediment flux becomes infinite. This system can be nondimensionalized (as denoted by an asterisk superscript) (*7*):

$$\zeta^* = \zeta / (S_C L_H) \quad \text{[S3a]}$$

$$x^* = x / L_H \quad \text{[S3b]}$$

$$U^* = U\left(\frac{2\rho^* L_H}{DS_C}\right) \quad \text{[S3c]}$$

$$t^* = t\left(D / L_H{}^2\right) \quad \text{[S3d]}$$

Substituting Equation 2 into 1 and using these nondimensionalizing definitions leads to the following solution for hillslope form:

$$\frac{d\zeta^*}{dt^*} = -\frac{d}{dx}\left(\left[\frac{d\zeta^*}{dx^*}\right]\left[1-\left|\frac{d\zeta^*}{dx^*}\right|^2\right]^{-1}\right) + \frac{1}{2}U^* \quad \text{[S4]}$$

which we use to model the evolution of a 1D hillslope through time.

Topographic Analysis

Roering, et al. (*7*) provide steady state solutions (i.e. when the condition $U=E$ is satisfied) for the above model which allow derivation of non-dimensional erosion rate E^* which is proportional to E (Equation 3c). The solutions also predict E^* based on quantifiable

hillslope topographic metrics, namely hilltop curvature C_{HT} [L^{-1}], hillslope length L_H [L] and mean hillslope gradient S [L/L]:

$$E^* = E\left(\frac{2\rho^* L_H}{DS_C}\right) \quad \text{[S5a]}$$

$$E^* = \frac{2C_{HT}L_H}{S_C} \quad \text{[S5b]}$$

Dimensionless relief can be derived theoretically as a function of E^* and predicted from topography using S:

$$R^* = \frac{1}{E^*}\left\{\sqrt{1+\left(E^*\right)^2} - \ln\left(\frac{1}{2}\left[\sqrt{1+\left(E^*\right)^2}\right]\right) - 1\right\} \quad \text{[S6a]}$$

$$R^* = \frac{S}{S_C} \quad \text{[S6b]}$$

We use Equations 5b and 6b to quantify E^* and R^* from topographic data, selecting S_C = 0.8 so that the requirement $R^* < 1$ is met. Varying S_C does not change the overall distribution of E^* vs. R^* data derivbed from topography but will alter their absolute values. These metrics are expected to deviate from their steady-state predictions when a hillslope is undergoing a transient response to base-level change. Following Hurst, et al. (*2*) we located hilltops as the adjoining margins of drainage basins extracted at a range of stream orders. In DBPR we restricted our analysis to interfluves trending roughly perpendicular to SAF, so that the hilltops are likely to be experiencing similar erosion rates on both sides of the divide (Fig. 1a). Using a 0.25m digital elevation model, we calculated the aspect, gradient and curvature (Laplacian) of elevation from the coefficients of a 6-term quadratic surface fitted by least squares to all cells within a 2.5m window centered on the cell of interest. C_{HT} was sampled directly at hilltops then an aspect-driven, steepest descent trace was run from each hilltop pixel until a mask defining the channel network/valley fill was encountered. From this trace L_H and S were calculated (see Fig. S1).

DEM Preparation

There were two principal concerns when preparing a DEM for this analysis. Firstly, the raw LiDAR point cloud contained returns misclassified as ground originating from small shrubs bushes (Fig S2 and Fig S3). These were identified and preferentially smoothed. Secondly, hilltops on the Dragon's Back Pressure Ridge get extremely narrow (<2 m) where denudation is rapid, and so calculating reliable values for C_{HT} required analysis to check for scale dependency (Fig. S4).

We interpolated raw point cloud LiDAR returns (point density ~4 m^{-2}) to a 0.25 m^2 resolution grid using MCC-LiDAR (*13*). This algorithm identifies locations in the point cloud where returns coincide spatially and removes the highest of these points. We do not

use MCC-LiDAR to identify shrub vegetation since the algorithm is dependent on curvature, and hence has a tendency to misidentify sharp hilltops as vegetation. To remove bushes and shrubs, the gridded data was smoothed using a non-local means filtering algorithm (*14*). Filtering is based on the assumption of regularity; that in the neighbourhood of the pixel of interest there are neighbourhoods that should look similar and therefore these non-local neighbourhoods can be used to predict the value at the original pixel. A non-local approach to DEM smoothing is particularly appealing towards the goal of removing bushes/shrubs which can be considered positive, high frequency noise since unlike many filtering techniques it does not assume the noise is normally distributed, therefore we minimize smoothing of hilltops. Fig. S2 shows an example of the effect of the smoothing.

We justify interpolation to a 0.25 m^2 grid resolution by arguing that this allows the true location and elevations of point cloud data to be better spatially resolved in the gridded approximation of the surface. This fine resolution allows us to calculate curvature over smaller windows, which is essential for resolving the curvature of narrow hilltops. Typically topographic curvature is calculated over scales greater than the characteristic wavelength of high-frequency noise associated with surface roughness, for example due to pit-mound topography generated by tree throw (*15*). At DBPR positive surface noise associated to low relief vegetation was smoothed. Given that hilltops are narrow, we calculated curvature over much smaller spatial scales. We varied the scale from 0.75 m to 5 m to test for scale effects. In Fig. S4 we show four hilltops distributed along the length of DBPR, and the associated variation in C_{HT} and its standard deviation as the scale over which curvature was calculated varied. The selected hilltops are distributed along the length of DBPR, chosen to reflect the various stages in landform development. We observe that C_{HT} varies little with length scales above ~2.5m, except on the sharpest hilltops (Fig. S2(b)) and there is a significant reduction in the standard deviation at this scale. At this scale we see through high frequency noise in the landscape. The hilltop in Fig. S2(b) is extremely narrow and therefore with increasing length scale we are underestimating C_{HT}. This is an important limitation to our results since it alters the range of E^* in Fig. 2, compressing the data at high E^* and may be the cause of clustering. It is therefore possible that any relationship between E and C_{HT} becomes artificially non-linear at high E.

Uplift/Base-level Model

The hillslope model presented in Equation S4 was forward modeled through time, assuming that D = 0.0086 m^2 a^{-1} (*12*) and L_H = 30 m (Fig. 1), which allowed us to calculate R^* and E^* at each simulated non-dimensional model time (Equation S3d). We favored fixing L_H rather than developing a more complex 2D landscape evolution model to avoid having to model complex valley forming processes, particularly transitions from detachment to transport limited conditions and the initiation of debris-flow processes. Time-dependent dimensionless uplift U^* was idealized as a Gaussian function with duration t_{std}^* peaking at time t_{max}^* and maximum uplift U_{max}^* treated as model parameters:

$$U^* = \frac{2U_{\max}{}^* L_H}{DS_C} e^{-\left(\frac{t^* - t_{\max}{}^*}{t_{std}{}^*}\right)^2} \quad \text{[S7]}$$

Posterior probability densities for U^* and $t_{std}{}^*$ were then sampled using a Markov-Chain Monte Carlo (MCMC) method according to the misfit between measured values of R^* and E^* and those calculated at corresponding t^* values in the forward model (*16*) using a maximum likelihood estimator:

$$MLE = \prod_{i=1}^{n} \frac{1}{\sqrt{2\pi}\sigma_u} \exp\left[-\frac{\left(u_i^{meas} - u_i^{\mathrm{mod}}\right)^2}{2\sigma_u{}^2} \right] \quad \text{[S8]}$$

where n is the number of data points, u could be either E^* or R^* as a function of time (determined using a space for time substitution based on a fault slip rate of 33 mm yr^{-1}) (*8*), the superscripts *meas* and *mod* denote measured and modeled quantities, respectively, and σ_u is the standard deviation of E^* or R^* data. Values of the peak uplift and width of the Gaussian uplift curve were changed after each iteration of the MCMC 'chain' and then accepted or rejected using an acceptance criterion (see below). For each iteration, the two parameter values were changed from the last accepted parameter value, and this deviation was selected from a Gaussian probability distribution bounded by minimum and maximum parameter values. Following standard practice, the standard deviation of the Gaussian distribution of each parameter (peak uplift and uplift field width) is set so that the acceptance rate of each iteration is c. 33 % (*17*). This process is iterated upon several thousand times in order to constrain the posterior distribution of the model coefficients (*18*). The acceptance criterion is based on the Metropolis-Hastings algorithm (*19*). The likelihood of the current iteration is compared to the previous iteration. If the ratio likelihood of the new iteration to the previous iteration is > 1, then the new coefficient values are accepted. If this ratio is < 1, then the new coefficients are accepted with a probability equal to the ratio. To generate the posterior distribution of coefficient values, each iteration in the Markov Chain is weighted by the likelihood of the combination of parameter values, creating a probability distribution of each coefficient. This can be used to determine both mean and 95% credibility limits on the parameter values. The resulting best fit uplift field can be seen in Fig. 3.

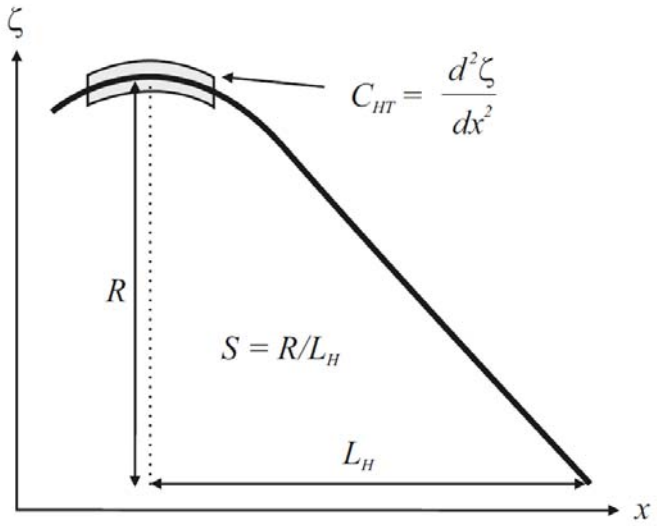

Fig. S1.

One dimensional schematic cross section of a hillslope showing the metrics extracted from topographic data. Relief R is the difference in elevation between the divide and the base of the hillslope, and the horizontal distance between these elevations is the hillslope length L_H. The ratio of these gives the mean hillslope gradient S. Hilltop curvature ($\nabla\zeta$ in 2D space) is the second derivative of the surface measure only at the divide.

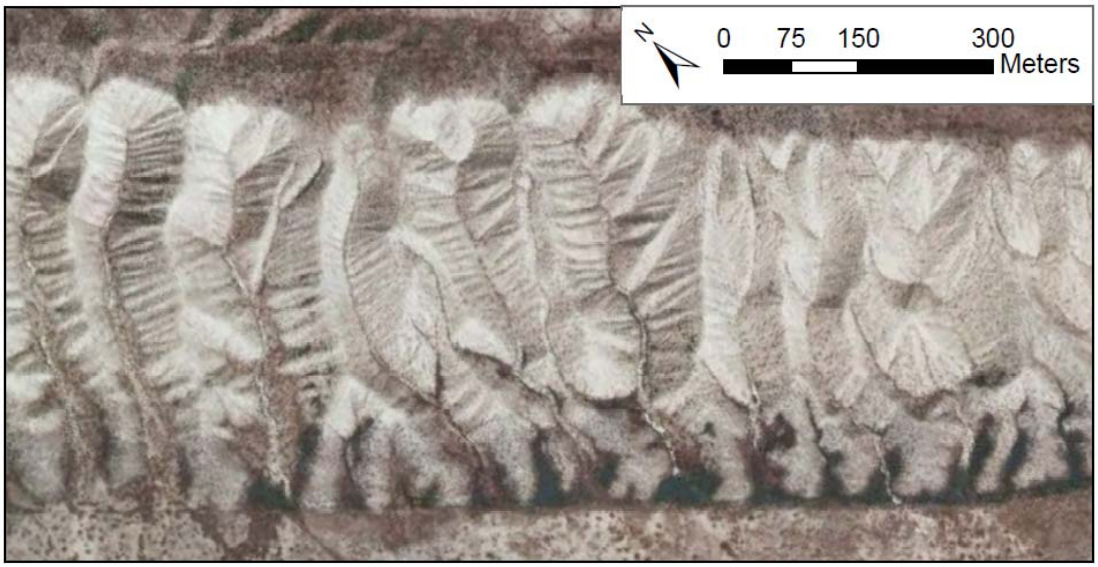

Fig. S2.

Aerial imagary (courtesy of Bing Maps) centered north-west of the zone of high uplift. Note that the hillslopes in this portion of the DBPR are corrugated which is interpreted to be due to small landslides/debris flows. Dark speckles are patchy shrub and brush vegetation which required filtering in the topographic data.

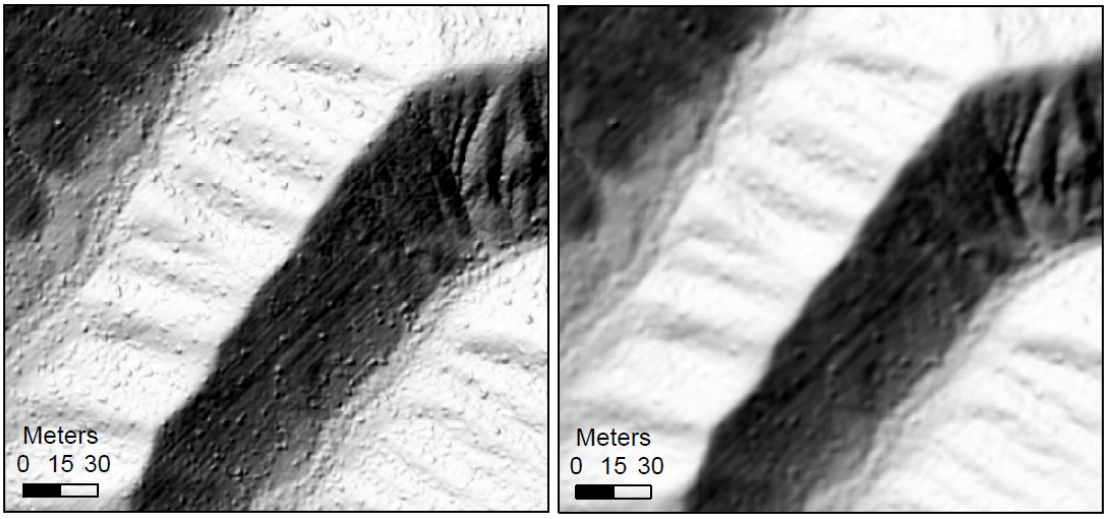

Fig. S3:

Example of smoothing by nonlocal means filtering algorithm which preferentially smoothes positive noise generated by the presence of local surface features such as bushes or boulders. Left image is topographic data gridded to 0.25m, right image is smoothed data using the nonlocal means techniques (*17*).

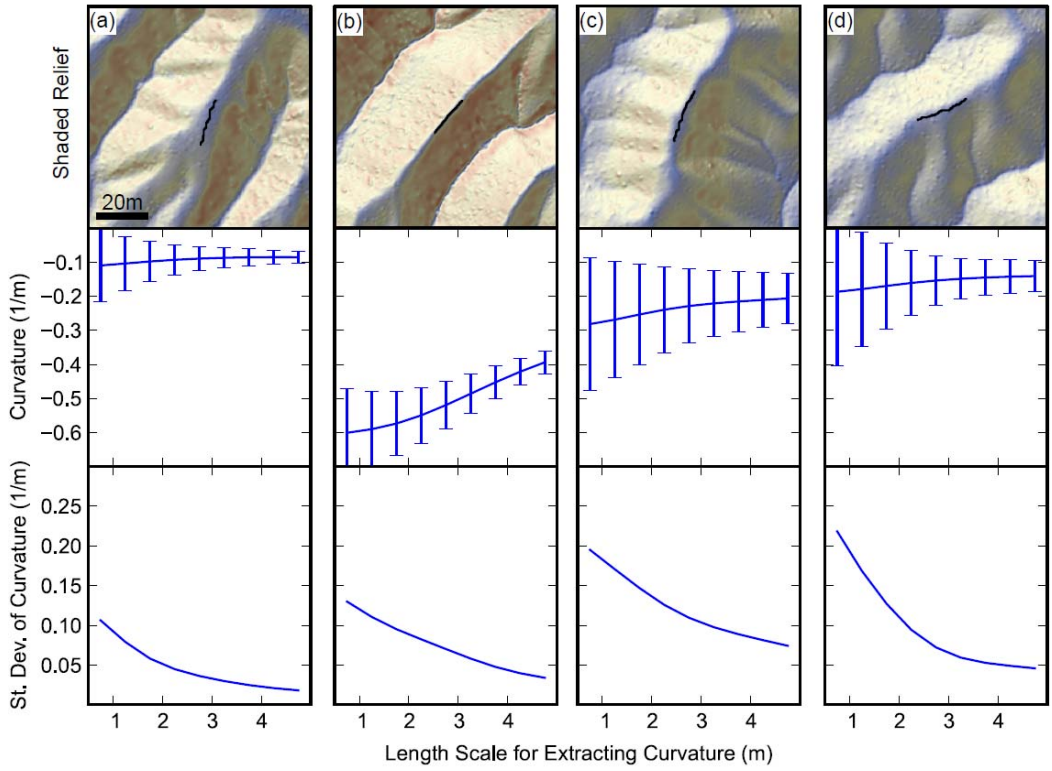

Fig. S4.

Variation in the Hilltop Curvature as a function of the length scale (or window size) over which curvature is extracted from the DEM. For each hilltop depicted in black in the shaded relief image, we extract the mean and standard deviation of curvature with a range of window sizes. Columns (a)-(d) are for hilltops distributed along the length of DBPR recording (a) transient response to uplift/erosion, (b) high erosion rate, steep planar hillslopes and narrow ridges, (c)-(d) relaxation of hillslope after uplift has ceased. For (a), (c) and (d) mean hilltop curvature is independent of window sizes above 2.5m so this is the scale we use. On sharp hilltops with steep side slopes (b) negative hilltop curvature increases as the window size decreases suggesting we will underestimate C_{HT} on such hilltops.